

# Revisiting stress-corrosion cracking and hydrogen embrittlement in 7xxx-Al alloys at the near-atomic-scale

Martí López Freixes <sup>1</sup>, Xuyang Zhou <sup>1</sup>, Huan Zhao <sup>1</sup>, H  l  ne Godin<sup>2</sup>, Lionel Peguet<sup>2</sup>, Timothy Warner<sup>2</sup> & Baptiste Gault <sup>1,3</sup> 

The high-strength 7xxx series aluminium alloys can fulfil the need for light, high strength materials necessary to reduce carbon-emissions, and are extensively used in aerospace for weight reduction purposes. However, as all major high-strength materials, these alloys can be sensitive to stress-corrosion cracking (SCC) through anodic dissolution and hydrogen embrittlement (HE). Here, we study at the near-atomic-scale the intra- and inter-granular microstructure ahead and in the wake of a propagating SCC crack. Moving away from model alloys and non-industry standard tests, we perform a double cantilever beam (DCB) crack growth test on an engineering 7xxx Al-alloy. H is found segregated to planar arrays of dislocations and to grain boundaries that we can associate to the combined effects of hydrogen-enhanced localised plasticity (HELP) and hydrogen-enhanced decohesion (HEDE) mechanisms. We report on a Mg-rich amorphous hydroxide on the corroded crack surface and evidence of Mg-related diffusional processes leading to dissolution of the strengthening  $\eta$ -phase precipitates ahead of the crack.

<sup>1</sup>Max-Planck-Institut f  r Eisenforschung GmbH, D  sseldorf, Germany. <sup>2</sup>C-TEC, Parc Economique Centr  al, Constellium Technology Center, Voreppe, Cedex, France. <sup>3</sup>Department of Materials, Royal School of Mines, Imperial College London, London, UK. email: [b.gault@mpie.de](mailto:b.gault@mpie.de)

The global need to achieve net-zero carbon emission reinforces the need for light and high-strength materials for e.g. lightweight vehicles and developing the infrastructure for a hydrogen economy in e.g. the commercial aircraft or iron-making sectors. The 7xxx series Al alloys are already extensively used for weight reduction purposes in aerospace<sup>1</sup> and are poised to see their usage widen. Cu-rich 7xxx series Al alloys have complex microstructures, including  $\eta/\eta$ -phase ( $\text{Mg}(\text{Zn}, \text{Cu}, \text{Al})_2$ ) hardening precipitates, dispersoids such as  $\text{Al}_3\text{Zr}$ , and coarse intermetallic particles such as  $\text{Al}_7\text{Cu}_2\text{Fe}$  and  $\text{Mg}_2\text{Si}$ <sup>2</sup>. These alloys are strengthened through precipitation of the solute-rich  $\eta$ -phase in the grain interior and at the grain boundary (GB). However, 7xxx Al alloys can be susceptible to hydrogen embrittlement (HE), particularly through generation of hydrogen during stress-corrosion cracking (SCC)<sup>3–7</sup>.

SCC is driven by both anodic dissolution and HE, but their relative contributions to SCC depend on the environment but also the alloy compositions, plate thicknesses and tempers<sup>3,4,8,9</sup>. Academic studies often focus on the effects of H on mechanical properties or its microstructural trapping<sup>10–15</sup> under conditions far from those encountered in operation, making them difficult to directly translate into practice. Despite extensive research on SCC and HE of these alloys<sup>3–7</sup>, a holistic, mechanistic understanding of these complex processes is still missing and this hinders the development of a materials design strategy to overcome these crucial issues.

Atomic H is produced at crack tips as a consequence of corrosion<sup>16</sup> mostly arising from differences in potential between the  $\eta$ -phase, Al-rich matrix<sup>17</sup> and the GB region, and is hence indissociable from SCC. HE has been associated to hydrogen-enhanced localised plasticity (HELP) and hydrogen-enhanced decohesion (HEDE) of GBs amongst others<sup>7,11,18</sup>. The HELP mechanism is based on an observed increase in dislocation motion and slip localisation in the presence of H in solid solution<sup>18</sup>, whereas HEDE proposes that the presence of H reduces the cohesive energy of interfaces, thereby reducing the fracture work<sup>11</sup>. A recent article proposed that HEDE is caused by the joint effect of H and Mg segregated to GBs<sup>13</sup>.

Artificial ageing, used to optimise properties, also alters the composition of the precipitates and their susceptibility to corrosion<sup>19,20</sup> and SCC<sup>5,6,9,21–23</sup>. Overageing introduces more Cu in the  $\eta$ -phase and increases its electrochemical potential and thus reduces the potential difference with the matrix and diminishes H generation at the cathodic sites, which has been associated with a reduced susceptibility to SCC<sup>5,24,25</sup>. Cracks caused by SCC propagate primarily intergranularly, and crack arrest markings (CAM) observed on fracture surfaces in chloride solutions<sup>4</sup> and humid air<sup>26</sup> indicate discontinuous cracking, which is inconsistent with a slip dissolution-type mechanism being rate-controlling<sup>3</sup> as sometimes proposed<sup>3,9</sup>. CAMs can be caused by a variety of SCC mechanisms, including film-induced cleavage, HEDE and adsorption-induced dislocation emission<sup>27</sup>.

The presence of CAMs suggests that all cracking-related phenomena occur locally, just ahead of the crack tip. In addition, the oxide produced by corrosion, and its relative stability determine the H production rate, its ingress and trapping are microstructure dependent. Yet, we lack spatially resolved H compositional data during SCC and there is very limited information reported on the composition and structure of the corroded layer formed at the tip of a propagating stress-corrosion crack in Al alloys. These knowledge gaps hinder the determination of the active mechanisms during SCC.

Here, we study the microstructural and microchemical changes caused by a propagating stress-corrosion crack at the nanoscale by using transmission-electron microscopy (TEM) and atom probe tomography (APT). APT has a high chemical and spatial

resolution, and provides accurate compositional information<sup>28</sup>. It has successfully been used to map trapped H in steels<sup>29</sup>, including at crystalline defects<sup>30</sup>, as well as in Ti-alloys<sup>31</sup>, in a 7xxx Al-alloy<sup>13</sup>, and to analyse crack tip oxides formed during SCC in stainless steels<sup>32</sup>. We focus on the direct vicinity of cracks and in regions ahead of the main crack, especially grain boundaries along which the crack is expected to grow. We observe the segregation of H to the GB ahead of the crack and on linear features usually attributed to dislocations. The corroded crack surface is a Mg-rich, chlorinated amorphous hydroxide. For clarity, we refer to it simply as oxide throughout. The composition of the precipitate-free zone (PFZ) and of precipitates near and ahead of the crack is vastly modified, and the matrix near the metal-oxide interface contains up to over 1 at% O, i.e. well above the solubility limit of O in Al, while no increased level of H is measured. We discuss our findings in perspective with the published literature and provide an array of discussion points relative to the interplay of structural defects and the transport of solutes from the matrix, possibly assisting with the dissolution of the strengthening phases, thereby changing the resistance against crack propagation.

## Results

**Sample characterisation far from the crack.** APT analyses of the commercial aluminium alloy 7449-T7651 from the GB and the grain interior away from the crack including,  $\eta$ -phase precipitates, matrix and PFZ are displayed in Supplementary Fig. 1. Features across multiple datasets show spread in their compositions, as plotted in Supplementary Fig. 1b, c. Mg and Zn levels within the  $\eta$ -phase precipitates from the grain interior and the near GB region display a linear relationship, with Mg ranging from 15 to 32 at.%, and Zn from 25 to 54 at.%. In turn, matrix and PFZ solute compositions exhibit an array of possible values. The mean Cu value for each of the features of interest are shown in Supplementary Fig. 1b, c. The average composition values of the matrix, PFZ and the  $\eta$ -phase GBP are reported in Table 1.

**Effect of H on deformation behaviour.** We performed an industry standard double cantilever beam (DCB) crack growth test to study the SCC behaviour of the alloy 7449-T7651. Following careful drying in an oven and storage in laboratory air for ~3 years, we investigated the crack tip region using (S)TEM. The crack is inter-granular and displays void-like features (Fig. 1b), suggested by Lynch<sup>7</sup> to be one of the crack propagating mechanisms. Energy-dispersive X-ray spectroscopy (EDS) confirms the presence of an oxide at the crack and within the voids, and the matrix adjacent to the crack oxide is devoid of precipitation (Supplementary Figs. 2, 3). The selected area electron diffraction pattern from the corroded crack indicates that the oxide is amorphous (Supplementary Fig. 4). Near the void-like features, we observed an array of dislocations (Fig. 1c), indicative

**Table 1** Calculated average values from the reference data shown in Supplementary Fig. 1b, c.

	Al	Zn	Mg	Cu
Matrix oxidised	94.13 ± 0.59	3.53 ± 0.34	1.63 ± 0.42	0.72 ± 0.09
2ndary crack				
PFZ (ref.)	99.68 ± 0.16	0.18 ± 0.04	0.08 ± 0.03	0.06 ± 0.03
Matrix (ref.)	98.47 ± 0.48	0.54 ± 0.16	0.19 ± 0.07	0.1 ± 0.07
GBP (ref.)	8.83 ± 1.26	49.2 ± 0.68	34.4 ± 0.54	7.53 ± 0.33

The reference GBP values correspond to the grain boundary containing dataset in Supplementary Fig. 1a. The values for the matrix solute content in the oxidised 2ndary crack are an average of the values presented in Fig. 3b. The error values reported correspond to the standard deviation of all measurements.

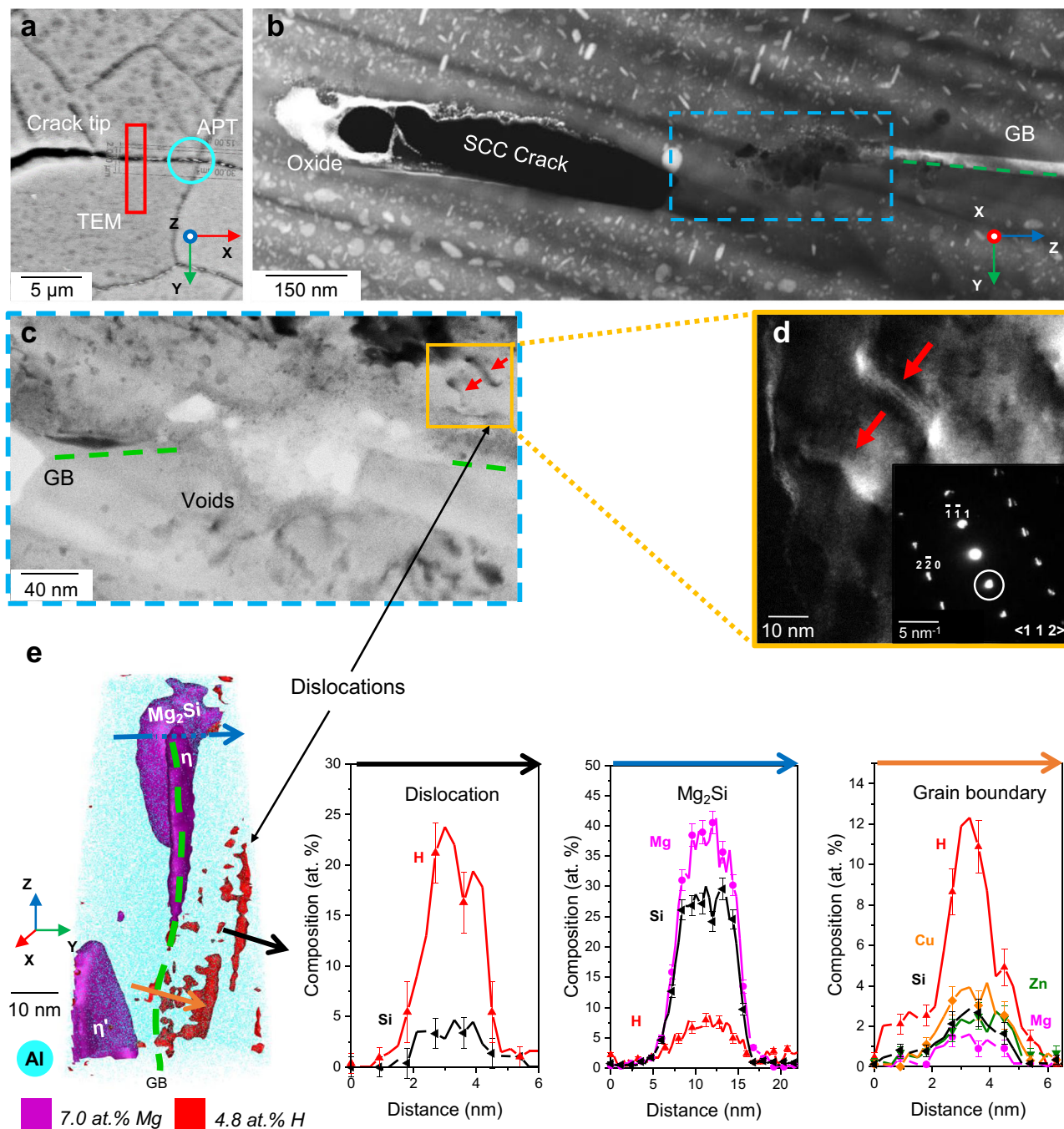


**Fig. 1** H effects on deformation behaviour near a stress-corrosion crack. **a** SEM micrograph of the SCC crack tip, showing the indicative locations of APT and TEM analysis. **b** STEM image of the crack tip region revealing the presence of oxide and void-like structures. **c** TEM BF image showing dislocations near the void region, pointed by the red arrows. **d** DF image corresponding to the (111) diffraction spot of the dislocations imaged in **b** pointed by the red arrows. **e** APT reconstruction of the GB 4 μm ahead of the crack showing the presence of dislocations with H and Si segregation. 1D Composition profiles across the GB, the dislocation and the Mg<sub>2</sub>Si particle, respectively measured along the arrows shown in the APT reconstruction. The error bars correspond to the standard deviation within each of the bins in the profile. Grain boundary (GB). Transmission-Electron Microscopy (TEM). Atom Probe Tomography (APT).

of plasticity, sitting on (111) planes, as confirmed by dark field TEM (Fig. 1d).

APT analysis was performed ~4 μm ahead of a crack tip (Fig. 1a). The dataset contains a GB with η/η'-phase precipitates as well as Mg<sub>2</sub>Si particles (Fig. 1e). The red set of iso-surfaces delineates regions of high H composition that form a planar array of elongated features typically associated with segregation to dislocations<sup>33</sup>. Based on atom probe crystallographic analysis, as

outlined in ref. <sup>34</sup> we confirmed that these features lie on a (111) plane, as expected for dislocations in the face-centred cubic Al-matrix, thereby supporting the hypothesis. The segregated H reaches locally near 20 at.%, along with ~4 at.% Si. H is also found segregated to the grain boundary and trapped within the Mg<sub>2</sub>Si particle sitting at the boundary (Fig. 1e). This is in line with recent reports of H segregation to grain boundaries in a 7xxx Al-alloy<sup>13</sup>. The observed segregation to the dislocations could thus be

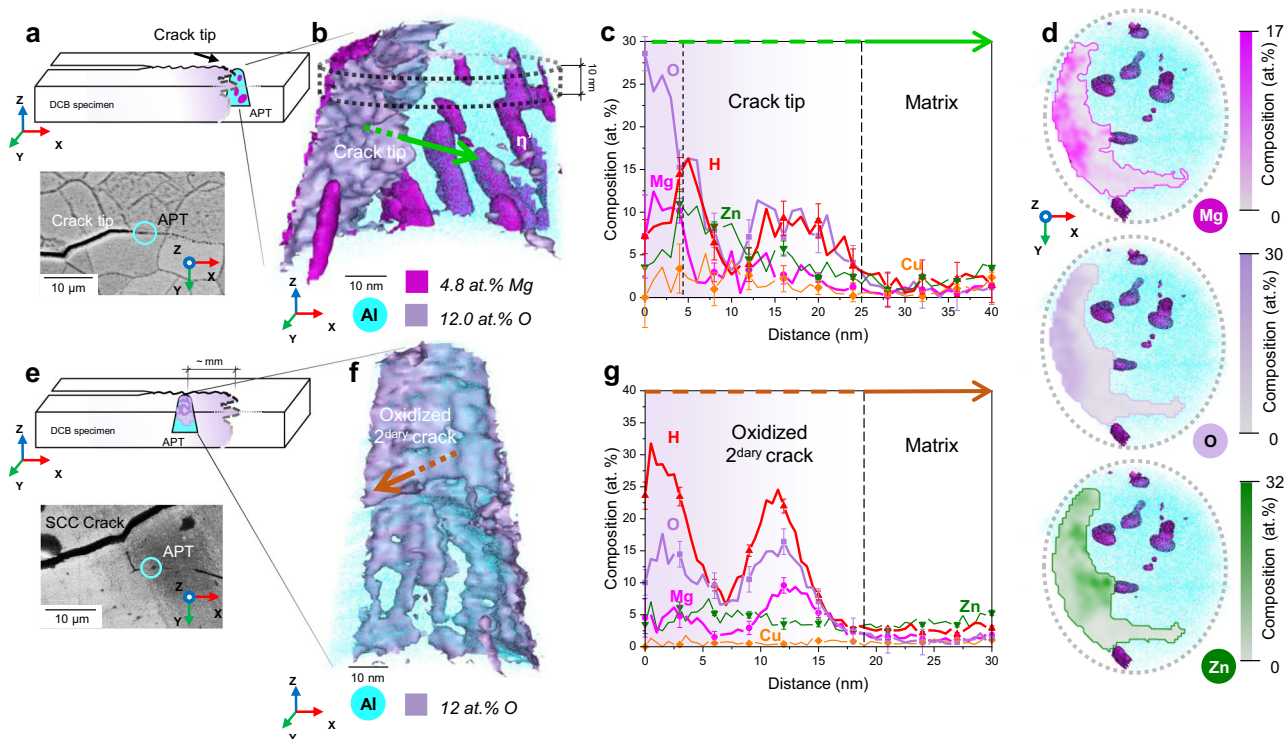


**Fig. 2** Corrosion behaviour during stress-corrosion cracking of the 7449-T7651 alloy. **a** Schematic of a DCB sample showing the APT crack tip sample location and orientation. **b** APT reconstruction of the crack tip of an SCC crack. **c** 1D composition profile across the oxide-matrix interface showing the oxide composition, measured within a 10 nm ( $\phi$ ) cylinder along the arrow in **b**. **d** 2D composition maps, obtained from a 10 nm slice, showing the 2D elemental distribution of Mg, O and Zn in the oxide within the dotted-line slice shown in **b**. **e** Schematic of a DCB sample showing the APT secondary crack sample location and orientation. **f** APT reconstruction of an oxidised secondary crack displaying the complex oxide morphology and absence of precipitation. **g** 1D composition profile across the oxide-matrix interface, measured within a 10 nm ( $\phi$ ) cylinder along the arrow in **f**. The error bars correspond to the standard deviation within each of the bins in the composition profiles shown. Double Cantilever Beam (DCB). Atom Probe Tomography (APT).

caused by the shearing through  $\text{Mg}_2\text{Si}$  particles, and both Si and H being dragged by, or subject to pipe diffusion along the dislocation connecting regions of different chemical potential<sup>35,36</sup>. H measurements by APT are notoriously challenging, because of the presence of H from the residual gas of the ultrahigh vacuum chamber<sup>29</sup>. The reliability of our measurements is further discussed below.

**On the crack oxide.** We targeted the tip of an SCC crack for specimen preparation along the main propagating crack in the DCB sample (Fig. 2a). Analysis of the desorption pattern (Supplementary Fig. 5) formed through the APT dataset (Fig. 2b) provided sufficient crystallographic information to determine the existence of two grains and thus of a GB within the reconstruction. We therefore assumed that we captured the tip of the actual propagating crack, as SCC cracks are known to propagate almost exclusively following an inter-granular mode in Al alloys<sup>3</sup>. As shown in Supplementary Fig. 5, the existence of two different desorption patterns in the dataset, as displayed by the distinct orientation of the crystallographic poles, indicates that there are in fact two different grains within the needle, with distinct crystallographic orientations. Therefore, a GB between the two grains was necessarily present in the needle before analysis. However, we could not locate the GB within the dataset, as no clear evidence of segregated solutes could be found, and there was a microfracture<sup>37</sup> during the data acquisition that could lead to a loss of information specifically in the GB region.

An iso-composition surface with an arbitrary threshold of 12 at.% O highlights the oxide-matrix interface, which exhibits a

very complex, rough morphology (Fig. 2b). Figure 2c plots the atomic ratios through the interface, along the suspected crack propagation direction. A two-layer structure appears, with first a  $\sim 5$  nm zone enriched in Mg and O, followed by a region with increased Zn and lower in O and Mg. O/H increase again further ahead, but Mg and Zn do not show increased levels. The formation of an Mg-rich oxide film in aluminium alloys was suggested by Green et al.<sup>38</sup> and reported experimentally<sup>39,40</sup>. The oxide film is also found to be hydrated, which is in line with previous observations<sup>3,39,41</sup>. Levels of Cl of up to 14 at.%, not included in the profiles for clarity, are also incorporated in the oxide film, as expected<sup>4</sup>. Cl enrichment is seemingly correlated to O, as shown in Supplementary Fig. 6a.

Two-dimensional compositional maps (Fig. 2d) from the top of the reconstructed APT dataset as indicated in Fig. 2b, and displayed top-down, highlight the inhomogeneity of the oxide and complement Fig. 2c. The enrichment of Mg and O is coincident, while Zn and Cu (Supplementary Fig. 7) appear to be accumulated at the oxide-metal interface. This suggests that Mg is being preferentially oxidised during corrosion of the freshly cracked surface. An Mg-rich and Zn-poor oxide and a Zn-rich, Mg-poor adjacent region is consistent with previous reports on oxidised  $\eta$ -phase precipitates<sup>25,42</sup>. We then performed APT analyses several mm in the wake of the crack tip, along an oxidised secondary crack (Fig. 2e), in order to reveal the solute distribution long after the crack has passed. It should be noted that we use the term “secondary crack” to define cracks that were not the main SCC crack. The tomographic reconstruction in Fig. 2f also evidences a complex morphology of the interface

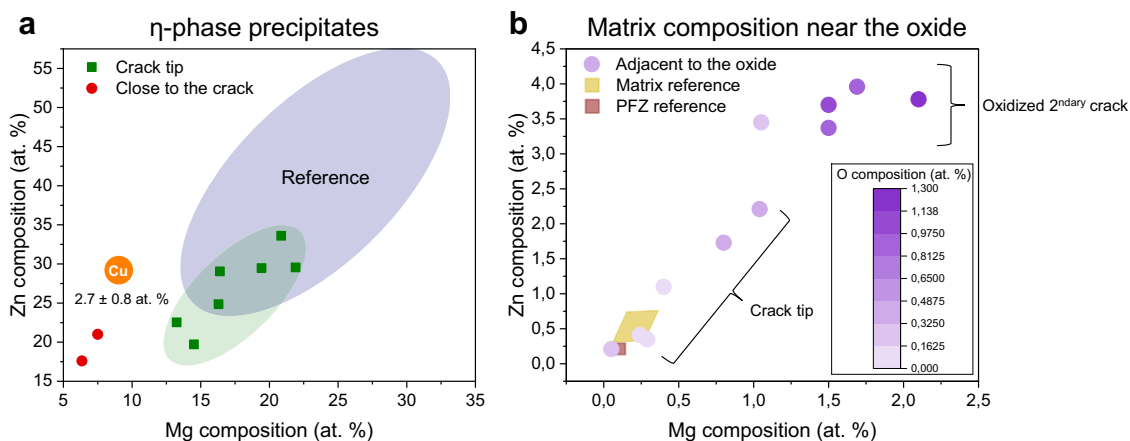


**Fig. 3 Matrix and  $\eta$ -phase precipitate compositional evolution during stress-corrosion cracking.** **a**  $\eta$ -phase precipitate composition around the crack tip and very close to the crack compared with reference values from Supplementary Fig. 1c. The composition of  $\eta$ -phase precipitates captured close to the crack, within 1  $\mu\text{m}$ , in another dataset are also added to the analysis. Cu average composition in the  $\eta$ -phase precipitates at the crack tip and close to the crack is also reported, also showing a marked decrease in Cu content with respect to reference values from Supplementary Fig. 1c. The error values reported for Cu correspond to the standard deviation of all measurements; **(b)** matrix composition around the crack tip and adjacent to the oxidised secondary crack compared with reference values from Supplementary Fig. 1b. Matrix O levels are also displayed at each data point. Please refer to Supplementary Fig. 8b for error values for O measurements. Precipitate-Free Zone (PFZ).

**Table 2 Nominal compositions for AA7449 (in at%, calculated from wt% nominals<sup>76</sup>).**

Al	Zn	Mg	Cu	Mn	Si	Fe	Zr + Ti
Bal.	3.55	2.65	0.8	0.1	0.06	0.05	0.06

between the metallic matrix and the oxidised crack. A composition profile perpendicular to the oxide/metal interface (Fig. 2g) shows the highly inhomogeneous oxide composition, with H levels reaching up to 30 at.% in the film, and with O/H peaks coinciding with Mg peaks. Conversely, Zn and Cu display no partitioning. It should be noted that Cl levels in the oxide film are much lower than at the crack tip, as shown in Supplementary Fig. 6. This might be caused by the lower pH at the crack tip, which has been correlated to increased Cl content in the oxide film<sup>4</sup>. The adjacent matrix is devoid of precipitates, as observed also by STEM-EDS (Fig. 1 and Supplementary Fig. 2). This motivated an analysis of the composition of the  $\eta$ -phase precipitates around the crack tip (Fig. 3a) that reveals a lower solute content than expected. The Mg content decreases down to 13 at.% and Zn levels to 20 at.% within the precipitates, on average leaner in solute compared to the reference composition reported in Supplementary Fig. 1b. The behaviour of Cu is similar to Mg and Zn, with Cu levels going from 7.3 at.% in the reference measurements (Supplementary Fig. 1b) to 2.7 at.% in the  $\eta$ -phase precipitates around the crack tip (Fig. 3a). The precipitates' dissolution leads to a significant increase in the matrix composition (Fig. 3b), up to tenfold across different locations around the crack tip with respect to the undeformed reference (Supplementary Fig. 1a). This is also observed in the matrix adjacent to the oxidised secondary crack (Fig. 3b and Table 1), where the composition is close to the alloy's nominal composition (Table 2), except for Mg, which has leached to the oxide layer. The matrix composition in the vicinity of the crack tip bridges the gap between the near-crack region and the reference data, hinting at a transient precipitate dissolution process (Fig. 3b). The variation in the matrix compositions is notably higher than in the reference measurements and no correlation between the solute enrichment and the distance to the captured oxides could be established. We also quantified the O dissolved in the matrix

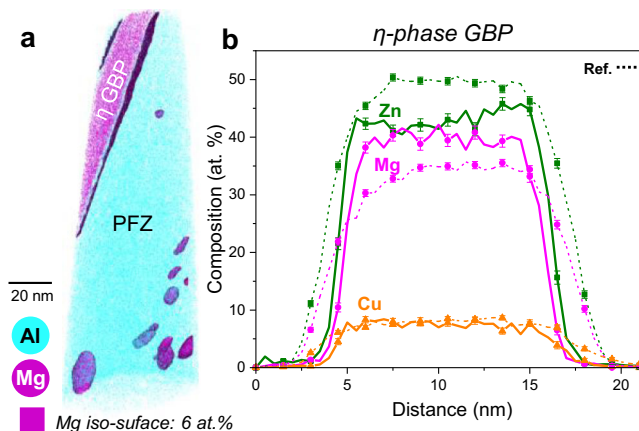


**Fig. 4 Compositional fluctuation on the grain boundary ahead of the stress-corrosion crack.** **a** APT reconstruction of the grain boundary ahead of the crack; **b** Composition profile showing a  $\eta$ -phase grain boundary precipitate with an Mg composition increased with respect to the 33 at.% dictated by the stoichiometry of the  $\text{Mg}(\text{Zn}, \text{Cu}, \text{Al})_2$  phase. The error bars correspond to the standard deviation within each of the bins in the profile. The displayed reference values are measured across the GBP shown in Supplementary Fig. 1a, with the average composition values shown in Table 1. Grain Boundary Precipitate (GBP). Precipitate-Free Zone (PFZ).

which, to a first approximation, scales with the increasing matrix solute content, as reported by the colour change of the symbols in Fig. 3b, and is far above the expected content<sup>43</sup>.

**Composition fluctuations ahead of the crack.** APT analyses near or at the grain boundary ahead of the crack yielded more evidence of the dynamic behaviour of the microstructure during SCC. APT analysis of a  $\eta$ -phase grain boundary precipitate located  $\sim 2 \mu\text{m}$  ahead of the crack shows an increased Mg concentration with respect to the expected stoichiometry of  $\text{Mg}(\text{Zn}, \text{Cu}, \text{Al})_2$ . The analysis reveals 38 at.% Mg, 46 at.% Zn, and 7 at.% Cu on average through the whole precipitate, but with 40 at.% Mg being reached locally (Fig. 4). This difference is significant based on the standard deviations for a GBP measured in the reference sample (Table 1).

## Discussion

Our results provide evidence for H absorption and segregation to dislocations and GBs during SCC in 7xxx series aluminium alloys. HE caused by the ingress of H ahead of the crack tip generally causes a 'brittle' fracture surface appearance and CAMs<sup>44</sup>. The embrittling effect of H had been so far been proven indirectly<sup>45</sup>. In situ TEM experiments have shown that H promotes slip planarity, enhanced dislocation glide and a decreased flow stress<sup>46,47</sup>. H transport by dislocations was already proposed by Albrecht et al.<sup>48</sup> in 1982, but had not been directly measured in aluminium alloys, especially during SCC. We provide here (Fig. 1d) evidence of co-localisation of H and dislocations in an Al-alloy, indicative of segregation and/or localised transport. H segregating to dislocation cores and promoting slip localisation and H transport forms the ground of HELP, i.e. one of the prevalent HE models<sup>11,18,49</sup>, and our observations strongly suggest it that it is active during SCC. As samples are over 3 years old, H must have been deeply trapped by the dislocations, consistent with previous reports<sup>12</sup>.

In addition, we present evidence of H segregating to grain boundaries ahead of the crack during SCC (Fig. 1d), suggesting that HEDE could be contributing to the crack progression, reducing the grain boundary cohesion based on the mechanism proposed by Zhao et al.<sup>13</sup>. Since H was detected along the GB, within an Mg<sub>2</sub>Si intermetallic particle and at dislocations in the matrix near the grain boundary 4 µm ahead of the crack, H diffusion through the grain boundary must have occurred during the crack propagating or as the cracked surface oxidised.

The evolutions of the microstructure and microchemistry near a propagating SCC crack had not previously reported in Al-alloy, but are consistent with previous observations in other engineering alloys<sup>50–52</sup>. We evidence a specific behaviour for Mg compared to Zn and Cu. The distribution reported is after the solutes were given ample time to equilibrate at room temperature, as the samples were only analysed ~3 years after the tests. We did not measure an increased H content in the Al-matrix, but an increased O content in the solute-rich sub-oxide region. O solubility in Al is reported to be close to zero<sup>43</sup>. Vacancy injection during cationic oxide growth could play a role, but recent investigations report negligible vacancy-O binding energy<sup>53</sup>. The origin of this increased O solubility is unclear and the effects on the mechanical properties such increased O levels in Al are unknown. In e.g. Ti-alloys<sup>54</sup>, O is a known solid solution strengthener, and O-ingress during SCC was shown to impact local phase equilibrium and cause the precipitation of an embrittling phase<sup>52</sup>. This could have an influence on SCC performance, and hence be relevant to the cracking process, in particular as this is occurring locally, just ahead of the crack, adjacent to the growing oxide.

Al-oxide films at room temperature form by outward diffusion of Al<sup>3+</sup> ions, according to the Cabrera-Mott model and experimental measurements<sup>55,56</sup>. This requires a steady diffusion of atoms from the bulk through the immobile metal/oxide interface<sup>56</sup>. Cl ions present at the crack tip during the SCC test destabilise the oxide layer, thus increasing corrosion rates<sup>4</sup>. Here, we analysed the composition of the oxide formed at the tip and in the wake of an SCC crack in a 7xxx series Al alloy. We show that a preferential Mg oxidation is taking place during SCC, thus creating an Mg-rich and also H-rich amorphous oxide. Interestingly, the oxide composition is different to measurements by Auger spectroscopy on AA7010 in dry air or seawater, which consisted of an outer MgO layer and an inner Al<sub>2</sub>O<sub>3</sub><sup>57</sup>.

The Mg partitioning to the oxide provides a driving force for Mg diffusion in the near-crack region. Diffusion from the neighbouring matrix and along grain boundaries to the Mg-depleted region is hence expected upon the onset of corrosion,

thereby disturbing the local equilibria and causing dissolution of precipitates to feed the progressing crack and growing Mg-rich oxide. The inhomogeneous solute supply to the crack during oxidation results in compositional fluctuations within the oxide (Fig. 2g). Precipitate dissolution and solute transport to an oxidising surface, possibly accelerated by diffusion along defects, occurs readily in the absence of stress<sup>39,58</sup>. This was referred to as the "reservoir effect" by Young and Gleeson<sup>59</sup> and has been observed in other systems like Cr-containing Fe-based alloys<sup>60</sup> for instance. Precipitates can then be understood as potential solute sinks that are thermodynamically trapped as a result of the heat treatment.

The dissolution of η-phase precipitates would alter the mechanical properties of the material ahead of the crack. Locally, the shear stress would decrease as the precipitates' radii are diminished by dissolution, thus reducing the resistance to dislocation movement and also releasing previously pinned dislocations. Dislocations could provide fast diffusion pathways<sup>61</sup> for the solutes rejected to the matrix to support the growth of the oxide. In the matrix composition values adjacent to the oxidised secondary crack (Fig. 3b), Mg displays higher relative variation than Zn, which could indicate enhanced Mg diffusion to the crack along defects. However, none of the main alloying elements was observed at the dislocations imaged here (Fig. 1d), so their role in assisting diffusion cannot be assessed from the current data. H segregation to dislocation cores increases planar slip, and thus increases strain localisation<sup>15</sup>. If precipitates are being sheared by dislocations, this can accelerate their dissolution<sup>62,63</sup>.

Since crack propagation takes place mostly along or near to the GBs, these could also act as a fast solute diffusion pathway to drive solutes towards the crack. The increased Mg composition found in an η-phase precipitate suggests that accelerated solute diffusion is also occurring along the grain boundary (Fig. 4). Alani<sup>58</sup> found large Zn-rich precipitation on the GB after corrosion occurred on the adjacent surface, which would be consistent with the diffusion-induced dissolution and re-precipitation at the grain boundary. They attributed the anomalous GB precipitation to an enhanced GB diffusion caused by the exposure to humid air at a relatively high temperature.

As a result of the Mg preferential consumption during the growth of the oxide, a subsurface region of differing composition forms<sup>59,64</sup>, rich in Zn and Cu, and depleted in Mg. We did not try to perform a precise diffusion length analysis, as the actual depth of the subsurface layer cannot be readily obtained from the APT data presented here, which could potentially lead to error in discerning the actual mechanisms contributing to diffusion in this region. Similar APT observations of substantial compositional changes and associated dissolutions in oxidised and stressed regions in superalloys had previously been reported<sup>51,65</sup>. In Al alloys, if corrosion is occurring at a high enough temperature, Schwarzenböck et al., and Alani and Swann<sup>39,58</sup> show Zn-rich precipitates forming in this solute-rich subsurface region, following oxidation in high humidity environments at 70 °C and 80 °C respectively. These observations are consistent with Mg diffusion to the oxide, precipitate dissolution and re-precipitation, similarly to what they observed in the matrix. However, it appears dependent on alloy composition, i.e. the Zn/Mg ratio, as Schwarzenböck et al.<sup>39</sup> only found anomalous subsurface precipitation in the alloy with the higher Zn/Mg ratio (5.2). It should be noted that the materials used in ref. <sup>39</sup>, were industrially sourced, so differences can also arise from differing ageing practices, as a same temper (e.g. T7651) will correspond to different ageing times and temperatures for different alloy compositions, including because of through-thickness microstructural and compositional variations that can affect the oxidation behaviour and H uptake. Garner et al.<sup>66</sup> reported substantial difference

in  $\eta$ -phase composition and GB coverage in two different Al alloys, attributed to the quench sensitivity of each alloy.  $\eta$ -phase GB coverage and composition could also play a role in the alloy's corrosion behaviour and therefore in SCC susceptibility.

H and O quantification by APT are known challenges, due to the presence of residual gases in the analysis chamber, ingress during specimen preparation and surface contamination during specimen transport and analysis<sup>29,67,68</sup>. These spurious species can obscure the signal from H or O originating from the specimen itself<sup>29,67</sup>. Higher electric fields during the analysis tend to improve the reliability of the measurements<sup>29,31,67</sup>. To assess the validity of the H/O quantification, the strength of the electric field during the experiments was determined, which can be estimated by using the charge-state ratio of Al ( $N(\text{Al}^{2+})/(\text{Al}^+)$ ) as a proxy<sup>69,70</sup>. Supplementary Fig. 8a shows the H concentration at different features reported herein, plotted against  $N(\text{Al}^{2+})/(\text{Al}^+)$ . H measurements on undeformed regions far from the crack, drawn and cold-rolled pure Al, and a  $\Sigma 3$  GB in an Al bi-crystal were included as reference. The H levels found in the crack, the GB, the dislocation and the  $\text{Mg}_2\text{Si}$  particle represent a marked increase with respect to the reference values at comparable field strengths, and with specimens prepared under the same conditions. Similarly, O values in the matrix adjacent to the oxide are plotted against the field strength in Supplementary Fig. 8b. It is thus clear that the increased H- and some of the O levels reported are not caused by a local drop in the electric field strength increasing residual gas adsorption from the chamber<sup>67</sup>, and originate from a difference in the materials' composition arising from the SCC or the processing<sup>71</sup>.

In summary, we have studied the consequences on the microchemistry and microstructure of the propagation of a stress-corrosion crack in a 7xxx Al-alloy, as well as the role of  $\eta$ -phase precipitates in assisting corrosion at the crack tip. The detection of aligned sets of dislocations carrying high content of H suggest strain localisation that can also assist both with precipitate dissolution and with crack propagation, according to the HELP mechanism<sup>18</sup>. H is also found segregated to GBs, which can reduce its cohesion and promote cracking, as stated by the HEDE mechanism<sup>11,13</sup>. In addition, we report on a hydrated, Mg-rich, non-stoichiometric Al-oxide. The growth of the oxide drives leaching of Mg from the alloy, and this localised preferential oxidation in the vicinity of the crack produces a strong redistribution of the solutes, leading to precipitate dissolution. Dislocations, along with grain boundaries, also offer a path for accelerated diffusion of solutes towards the growing oxide and hence the precipitate dissolution process.

We cannot yet provide a clear answer as to whether the reported precipitate dissolution process plays a direct role in the cracking mechanism by modifying the local resistance against further crack propagation, or if it occurs concomitantly, accelerating H production and absorption by supplying more reactive solutes to the oxidising surface. Should this be found to contribute to SCC, it would be consistent with the empirical evidence that overaging reduces crack growth rates, since it increases precipitate size and pulls solutes out of the matrix, thus rendering the oxidation, precipitate dissolution and solute redistribution processes all slower. We also reported the presence of a high concentration of O and of the main solutes in the matrix in the vicinity of the propagating crack. The possible influence of this addition of O on the local strength and other material properties remains unclear.

It is also a possibility that some of the features observed have occurred post-mortem, as the sample was close to 3 years old at the time of analysis. However, the authors could not rationalise this hypothesis based on the current available literature. It is also possible that the crack was blunted and that therefore the

observations reported herein are not representative of the cracking process, but the crack growth rate at the moment the SCC test was stopped was near  $10^{-9}$  cm/s, in accordance with ASTM G168-17<sup>72</sup>. Knight et al.<sup>9</sup> performed measurements of CAM spacing at high and low stress intensity values, corresponding to higher and lower crack growth rates, respectively. They did not find any effect of stress intensity, i.e. of crack growth rate, on average CAM spacings in a variety of different alloys and tempers, strongly indicating that the cracking mechanism is the same regardless of the crack growth rate and stress intensity value.

We aim to perform further measurements on a different set of samples to confirm or refute the results presented herein. Yet these observations raise numerous questions that should motivate further research, in particular if the microstructure evolves and solute redistributes during SCC of 7xxx Al alloys in humid air. These insights will be precious to help refine existing models and improve their predictive capabilities.

## Methods

**SCC testing.** We conducted a double cantilever beam (DCB) crack growth test on specimens machined in the S-L orientation from the mid-thickness of 75 mm 7449-T7651 plate supplied by Constellium. Before the test, the surface was thoroughly wiped with acetone and subjected to ultrasound cleaning. Testing was carried out according to ASTM G168-17<sup>72</sup> at room temperature in laboratory air. Pre-cracking was done manually by 'pop-in' and droplets of 3.5% NaCl solution were added twice a day in the slit during weekdays. The DCB test was carried out in Constellium's laboratory in accordance with ASTM G168-17<sup>72</sup>. The sample was then dried in a drying oven and then stored in laboratory air for nearly 3 years before the microstructural characterisation was performed.

**Specimen preparation.** TEM and APT specimens were prepared from the crack tip and the grain boundary ahead using a FEI Helios Xe-Plasma focused ion beam (PFIB), as Ga is known to cause GB embrittlement and quantification issues in aluminium<sup>73</sup>. APT specimens were prepared following a site-specific preparation procedure<sup>74</sup> and the final cleaning voltage/current for the TEM foil was 5 kV/10 pA.

**Atom probe tomography.** APT analyses were performed on a Cameca Instrument Inc. Local Electrode Atom Probe (LEAP) 5000 XR (reflectron fitted) in voltage-pulsing mode, with a 20% pulse fraction at a pulsing rate of 125 kHz, with the specimen at a base temperature of 75, and with 4 ions detected per 1000 pulses on average. The non-oxide containing specimens were acquired at 40 K, 0.5% detection rate, 20% pulse fraction and 200 kHz pulse rate. APT reconstruction and analysis were performed using the CAMECA software AP Suite 6.1 and reconstructions were calibrated using crystallographic features<sup>75</sup>.

**Transmission-electron microscopy.** (S)TEM analysis was carried out in a JEOL JEM-2200FS operated at 200 kV.

## Data availability

The datasets generated during and/or analysed during the current study are available from the corresponding author.

Received: 14 March 2022; Accepted: 6 July 2022;

Published online: 25 July 2022

## References

1. Warner, T. Recently-developed aluminium solutions for aerospace applications. *Mater. Sci. Forum* **519–521**, 1271–1278 (2006).
2. Hatch, J. E. *Aluminum: Properties and Physical Metallurgy* (ASM International, 1984).
3. Holroyd, N. J. H. Environment-induced cracking of high-strength aluminum alloys. In *Proceedings of Environment-induced cracking of metals* (eds Gangloff, R. P. & Ives M. B.) 311–345 (NACE, Houston, TX, 1990).
4. Holroyd, N. J. H. & Scamans, G. M. Stress corrosion cracking in Al-Zn-Mg-Cu aluminum alloys in saline environments. in *Metallurgical and Materials Transactions A: Physical Metallurgy and Materials Science* vol. 44 1230–1253 (Springer, 2013).

5. Knight, S. P., Birbilis, N., Muddle, B. C., Trueman, A. R. & Lynch, S. P. Correlations between intergranular stress corrosion cracking, grain-boundary microchemistry, and grain-boundary electrochemistry for Al-Zn-Mg-Cu alloys. *Corros. Sci.* **52**, 4073–4080 (2010).
6. Young, G. A. & Scully, J. R. The effects of test temperature, temper, and alloyed copper on the hydrogen-controlled crack growth rate of an Al-Zn-Mg-(Cu) alloy. *Metall. Mater. Trans. A Phys. Metall. Mater. Sci.* **33**, 101–115 (2002).
7. Lynch, S. P. Environmentally assisted cracking: Overview of evidence for an adsorption-induced localised-slip process. *Acta Metall.* **36**, 2639–2661 (1988).
8. Schwarzenböck, E. et al. Environmental cracking performance of new generation thick plate 7000-T7x series alloys in humid air (Elsevier, 2020).
9. Knight, S. P. et al. Some effects of alloy composition on stress corrosion cracking in Al-Zn-Mg-Cu alloys. *Corros. Sci.* **98**, 50–62 (2015).
10. Scully, J. R., Young, G. A. & Smith, S. W. Hydrogen embrittlement of aluminum and aluminum-based alloys. *Gaseous Hydrogen Embrittlement of Materials in Energy Technologies: The Problem, its Characterisation and Effects on Particular Alloy Classes* 707–768 <https://doi.org/10.1533/9780857093899.3.707> (2012).
11. Robertson, I. M. et al. Hydrogen embrittlement understood. *Metall. Mater. Trans. B Process. Metall. Mater. Process. Sci.* **46**, 1085–1103 (2015).
12. Moshtaghi, M., Safyari, M., Kuramoto, S. & Hojo, T. Unraveling the effect of dislocations and deformation-induced boundaries on environmental hydrogen embrittlement behavior of a cold-rolled Al-Zn-Mg-Cu alloy. *Int. J. Hydrog. Energy* **46**, 8285–8299 (2021).
13. Zhao, H. et al. Hydrogen trapping and embrittlement in high-strength Al-alloys. *Nature* <https://doi.org/10.1038/s41586-021-04343-z> (2022).
14. Bhuiyan, M. S. et al. Combined microtomography, thermal desorption spectroscopy, X-ray diffraction study of hydrogen trapping behavior in 7XXX aluminum alloys. *Mater. Sci. Eng. A* **655**, 221–228 (2016).
15. Su, H. et al. Influence of hydrogen on strain localization and fracture behavior in Al Zn Mg Cu aluminum alloys. *Acta Mater.* **159**, 332–343 (2018).
16. Scully, J. R., Young, G. A. & Smith, S. W. Hydrogen embrittlement of aluminum and aluminum-based alloys. in *Gaseous Hydrogen Embrittlement of Materials in Energy Technologies: The Problem, its Characterisation and Effects on Particular Alloy Classes* 707–768 (Elsevier Ltd., 2012). <https://doi.org/10.1533/9780857093899.3.707>.
17. Buchheit, R. G. A Compilation of Corrosion Potentials Reported for Intermetallic Phases in Aluminum Alloys. *J. Electrochem. Soc.* **142**, 3994 (1995).
18. Birnbaum, H. K. & Sofronis, P. Hydrogen-enhanced localized plasticity—a mechanism for hydrogen-related fracture. *Mater. Sci. Eng. A* **176**, 191–202 (1994).
19. Rometsch, P. A., Zhang, Y. & Knight, S. Heat treatment of 7xxx series aluminium alloys—Some recent developments. *Trans. Nonferrous Met. Soc. China* **24**, 2003–2017 (2014).
20. Andreatta, F., Terryn, H. & De Wit, J. H. W. Corrosion behaviour of different tempers of AA7075 aluminium alloy. *Electrochim. Acta* **49**, 2851–2862 (2004).
21. RAO, A. C. U., VASU, V., GOVINDARAJU, M. & SRINADH, K. V. S. Stress corrosion cracking behaviour of 7xxx aluminium alloys: a literature review. *Trans. Nonferrous Met. Soc. China* **26**, 1447–1471 (2016).
22. Goswami, R., Lynch, S., Holroyd, N. J. H., Knight, S. P. & Holtz, R. L. Evolution of grain boundary precipitates in Al 7075 upon aging and correlation with stress corrosion cracking behavior. *Metall. Mater. Trans. A* **44**, 1268–1278 (2012).
23. Chen, S. Y., Chen, K. H., Dong, P. X., Ye, S. P. & Huang, L. P. Effect of heat treatment on stress corrosion cracking, fracture toughness and strength of 7085 aluminum alloy. *Trans. Nonferrous Met. Soc. China* **24**, 2320–2325 (2014).
24. Zhao, H. et al. Segregation assisted grain boundary precipitation in a model Al-Zn-Mg-Cu alloy. *Acta Mater.* **156**, 318–329 (2018).
25. Ramgopal, T., Schmutz, P. & Frankel, G. S. Electrochemical Behavior of Thin Film Analogs of Mg (Zn, Cu, Al) 2. *J. Electrochem. Soc.* **148**, B348 (2001).
26. Holroyd, N. J. H. & Scamans, G. M. Crack propagation during sustained-load cracking of Al-Zn-Mg-Cu aluminum alloys exposed to moist air or distilled water. *Metall. Mater. Trans. A Phys. Metall. Mater. Sci.* **42**, 3979–3998 (2011).
27. Lynch, S. P. Progression markings, striations, and crack-arrest markings on fracture surfaces. *Mater. Sci. Eng. A* **468–470**, 74–80 (2007).
28. Gault, B. et al. Atom probe tomography. *Nat. Rev. Methods Prim.* **1**, 1–30 (2021).
29. Breen, A. J. et al. Solute hydrogen and deuterium observed at the near atomic scale in high-strength steel. *Acta Mater.* **188**, 108–120 (2020).
30. Chen, Y.-S. et al. Observation of hydrogen trapping at dislocations, grain boundaries, and precipitates. *Science* **367**, 171–175 (2020).
31. Chang, Y. et al. Characterizing solute hydrogen and hydrides in pure and alloyed titanium at the atomic scale. *Acta Mater.* **150**, 273–280 (2018).
32. Persaud, S. Y., Smith, J. M., Langelier, B., Capell, B. & Wright, M. D. An atom probe tomography study of Pb-caustic SCC in alloy 800. *Corros. Sci.* **140**, 159–167 (2018).
33. Kuzmina, M., Herbig, M., Ponge, D., Sandlobes, S. & Raabe, D. Linear complexions: Confined chemical and structural states at dislocations. *Science* **349**, 1080–1083 (2015).
34. Gault, B. et al. Advances in the reconstruction of atom probe tomography data. *Ultramicroscopy* **111**, 448–457 (2011).
35. Wu, X. et al. Unveiling the Re effect in Ni-based single crystal superalloys. *Nat. Commun.* **11**, 1–13 (2020).
36. Love, G. R. Dislocation pipe diffusion. *Acta Metall.* **12**, 731–737 (1964).
37. Gault, B., Moody, M. P., Cairney, J. M. & Ringer, S. P. *Atom Probe Microscopy*. vol. 160 (Springer New York, 2012).
38. Green, J. A. S., Viswanadham, R. K., Sun, T. S. & Montague, W. G. Grain boundary segregation and stress corrosion cracking of aluminium alloys. In *Corrosion/77, Proceedings of the International Corrosion Forum*, Paper 17, pp. 17/1–17/12 (NACE, San Francisco, California, 1977).
39. Schwarzenböck, E. et al. Evolution of surface characteristics of two industrial 7xxx aluminium alloys exposed to humidity at moderate temperature. *Surf. Interface Anal.* **51**, 1288–1297 (2019).
40. Wakefield, G. R. & Sharp, R. M. The composition of oxides formed on Al-Mg alloys. *Appl. Surf. Sci.* **51**, 95–102 (1991).
41. Hart, R. K. TKE FORMATION OF FILMS ON ALUMINIUM IMMersed IN WATER. *Trans. Faraday Soc.* **53**, 1020–1027 (1957).
42. Han, J. & Ogle, K. Editors’ choice—dealloying of MgZn<sub>2</sub> intermetallic in slightly alkaline chloride electrolyte and its significance in corrosion resistance. *J. Electrochem. Soc.* **164**, C952 (2017).
43. Krumnacker, O., Knacke, M. & Kubaschewski, O. The Al-O (Aluminum-Oxygen) system. *Bull. Alloy Phase Diagr.* **1985** **6**, 548–553 (1985).
44. Lynch, S. P. Metallographic and fractographic techniques for characterising and understanding hydrogen-assisted cracking of metals. *Gaseous Hydrogen Embrittlement of Materials in Energy Technologies: The Problem, its Characterisation and Effects on Particular Alloy Classes* 274–346 <https://doi.org/10.1533/9780857093899.2.274> (2012).
45. Ratke, L. & Gruhl, W. Modellversuch zum Mechanismus der Spannungsrisskorrosion von AlZnMg-Legierungen. *Mater. Corros.* **31**, 768–773 (1980).
46. Ferreira, P. J., Robertson, I. M. & Birnbaum, H. K. Hydrogen effects on the character of dislocations in high-purity aluminum. *Acta Mater.* **47**, 2991–2998 (1999).
47. Bond, G., Robertson, I. & Birnbaum, H. Effects of hydrogen on deformation and fracture processes in high-purity aluminium. *Acta Metall.* **36**, 2193–2197 (1988).
48. Albrecht, J., Bernstein, I. M. & Thompson, A. W. Evidence for dislocation transport of hydrogen in aluminum. *Metall. Trans. A* **13A**, 811–820 (1982).
49. Lu, G., Zhang, Q., Kioussis, N. & Kaxiras, E. Hydrogen-enhanced local plasticity in aluminum: an ab initio study. *Phys. Rev. Lett.* **87**, 095501 (2001).
50. Meisnar, M., Moody, M. & Lozano-Perez, S. Atom probe tomography of stress corrosion crack tips in SUS316 stainless steels. *Corros. Sci.* **98**, 661–671 (2015).
51. Kontis, P. et al. Microstructural degradation of polycrystalline superalloys from oxidized carbides and implications on crack initiation. *Scr. Mater.* **147**, 59–63 (2018).
52. Joseph, S. et al. A cracking oxygen story: a new view of stress corrosion cracking in titanium alloys. *Acta Mater.* **227**, 117687 (2022).
53. Ross, A. J., Fang, H. Z., Shang, S. L., Lindwall, G. & Liu, Z. K. A curved pathway for oxygen interstitial diffusion in aluminum. *Comput. Mater. Sci.* **140**, 47–54 (2017).
54. Yu, Q. et al. Origin of dramatic oxygen solute strengthening effect in titanium. *Science* **347**, 635–639 (2015).
55. Cabrera, N. & Mott, N. F. Theory of the oxidation of metals. *Rep. Prog. Phys.* **12**, 163 (1949).
56. Guise, O., Levy, J. & Yates, J. T. Direct measurement of the direction of interface motion in the oxidation of metals and covalent solids—Al(111) and Si(100) oxidation with O<sub>2</sub> at 300 K. *Thin Solid Films* **496**, 426–430 (2006).
57. Puiggali, M. et al. Effect of microstructure on stress corrosion cracking of an Al-Zn-Mg-Cu alloy. *Corros. Sci.* **40**, 805–819 (1998).
58. Alani, R. & Swann, P. R. Water vapour embrittlement and hydrogen bubble formation in Al-Zn-Mg Alloys. *Br. Corros. J.* **12**, 80–85 (1977).
59. Young, D. J. & Gleeson, B. Alloy phase transformations driven by high temperature corrosion processes. *Corros. Sci.* **44**, 345–357 (2002).
60. Durham, R. N., Gleeson, B. & Young, D. J. Factors affecting chromium carbide precipitate dissolution during alloy oxidation. *Oxid. Met.* **1998** **501** **50**, 139–165 (1998).
61. Legros, M., Dehm, G., Arzt, E. & Balk, T. J. Observation of giant diffusivity along dislocation cores. *Science* **319**, 1646–1649 (2008).
62. Bai, S., Liu, Z., Zhou, X., Gu, Y. & Yu, D. Strain-induced dissolution of Cu-Mg co-clusters and dynamic recrystallization near a fatigue crack tip of an underaged Al-Cu-Mg alloy during cyclic loading at ambient temperature. *Scr. Mater.* **64**, 1133–1136 (2011).
63. Hutchinson, C. R., Loo, P. T., Bastow, T. J., Hill, A. J. & da Costa Teixeira, J. Quantifying the strain-induced dissolution of precipitates in Al alloy



- microstructures using nuclear magnetic resonance. *Acta Mater.* **57**, 5645–5653 (2009).
64. Wang, G., Gleeson, B. & Douglass, D. L. A diffusional analysis of the oxidation of binary multiphase alloys. *Oxid. Met.* **1991** **35**, 333–348 (1991).
  65. Kontis, P. et al. The role of oxidized carbides on thermal-mechanical performance of polycrystalline superalloys. *Metall. Mater. Trans. A* **49**, 4236–4245 (2018).
  66. Garner, A. et al. Multiscale analysis of grain boundary microstructure in high strength 7xxx Al alloys. *Acta Mater.* **202**, 190–210 (2021).
  67. Sundell, G., Thuvander, M. & Andrén, H. O. Hydrogen analysis in APT: methods to control adsorption and dissociation of H<sub>2</sub>. *Ultramicroscopy* **132**, 285–289 (2013).
  68. Yoo, S.-H. et al. Origins of the hydrogen signal in atom probe tomography: case studies of alkali and noble metals. *New J. Phys.* <https://doi.org/10.1088/1367-2630/AC40CD> (2021).
  69. Kingham, D. R. The post-ionization of field evaporated ions: a theoretical explanation of multiple charge states. *Surf. Sci.* **116**, 273–301 (1982).
  70. Lefebvre, W. et al. 3DAP measurements of Al content in different types of precipitates in aluminium alloys. *Surf. Interface Anal.* **39**, 206–212 (2007).
  71. Su, H. et al. Assessment of hydrogen embrittlement via image-based techniques in Al–Zn–Mg–Cu aluminum alloys. *Acta Mater.* **176**, 96–108 (2019).
  72. *ASTM G168-17, Standard Practice for Making and Using Pre-cracked Double Beam Stress Corrosion Specimens.* (ASTM International, 2017).
  73. Liliensten, L. & Gault, B. New approach for FIB-preparation of atom probe specimens for aluminum alloys. *PLoS ONE* **15**, e0231179 (2020).
  74. Thompson, K. et al. In situ site-specific specimen preparation for atom probe tomography. *Ultramicroscopy* **107**, 131–139 (2007).
  75. Gault, B. et al. Advances in the calibration of atom probe tomographic reconstruction. *J. Appl. Phys.* **105**, 034913 (2009).
  76. The Aluminum Association. *International Alloy Designations and Chemical Composition Limits for Wrought Aluminum and Wrought Aluminum Alloys* (The Aluminum Association, 2018).

## Acknowledgements

We thank U. Tezins, A. Sturm, M. Nellessen, C. Broß, and K. Angenendt for their technical support at the FIB/APT/SEM facilities at MPIE. We are grateful for fruitful discussions and help with experiments from Diana Koschel, Annabelle Rossetto, Marcel Glienke and Damien Connétable. B.G. acknowledges the financial support from the ERC-CoG-SHINE-771602. X.Z. is grateful for funding from the Alexander von Humboldt Stiftung.

## Author contributions

M.L.F. performed the APT experiments; X.Z. performed the (S)TEM microscopy; M.L.F. and B.G. wrote the paper; B.G. supervised the work; H.Z., H.G., L.P. and T.W. contributed to the scientific discussion of the results and reviewed the paper.

## Funding

Open Access funding enabled and organized by Projekt DEAL.

## Competing interests

The authors declare no competing interests.

## Additional information

**Supplementary information** The online version contains supplementary material available at <https://doi.org/10.1038/s41467-022-31964-3>.

**Correspondence** and requests for materials should be addressed to Baptiste Gault.

**Peer review information** *Nature Communications* thanks Tomas Martin, Suraj Persaud and Fabio Scenini for their contribution to the peer review of this work.

**Reprints and permission information** is available at <http://www.nature.com/reprints>

**Publisher's note** Springer Nature remains neutral with regard to jurisdictional claims in published maps and institutional affiliations.



**Open Access** This article is licensed under a Creative Commons Attribution 4.0 International License, which permits use, sharing, adaptation, distribution and reproduction in any medium or format, as long as you give appropriate credit to the original author(s) and the source, provide a link to the Creative Commons license, and indicate if changes were made. The images or other third party material in this article are included in the article's Creative Commons license, unless indicated otherwise in a credit line to the material. If material is not included in the article's Creative Commons license and your intended use is not permitted by statutory regulation or exceeds the permitted use, you will need to obtain permission directly from the copyright holder. To view a copy of this license, visit <http://creativecommons.org/licenses/by/4.0/>.

© The Author(s) 2022